A rational design combining morphology and charge-dynamic for hematite/nickel-iron oxide thin-layer photoanodes: insights on the role of the absorber/catalyst junction.

Michele Orlandi,†[a] Serena Berardi,‡*[a] Alberto Mazzi,† Stefano Caramori,‡ Rita Boaretto,‡ Francesco Nart,‡ Carlo A. Bignozzi,‡ Nicola Bazzanella,† Nainesh Patel,§ Antonio Miotello.†*

† Department of Physics, University of Trento, I-38123, Povo (Trento), Italy.

‡ Department of Chemical and Pharmaceutical Sciences, University of Ferrara, Via Fossato di Mortara 17-19, 44100, Ferrara, Italy.

§ Department of Physics, University of Mumbai, Vidyanagari, Santacruz (E), Mumbai 400 098, India.

Corresponding authors: michele.orlandi@unitn.it, serena.berardi@unife.it

[a] These authors contributed equally to the manuscript.

KEYWORDS: thin-layer photoanode, oxygen evolving catalyst, pulsed laser deposition, porous morphology, photoelectrosynthesis, adaptive junction, nickel iron oxide, impedance spectroscopy.

ABSTRACT

Water oxidation represents the anodic reaction in most of the photoelectrosynthetic set-ups for artificial photosynthesis developed so far. The efficiency of the overall process strongly depends on the joint exploitation of good absorber domains and interfaces with minimized recombination pathways. To this end, we report on the effective coupling of thin layer hematite with amorphous porous nickel-iron oxide catalysts prepared *via* pulsed laser deposition. The rational design of such composite photoelectrodes leads to the formation of a functional adaptive junction, with enhanced photoanodic properties with respect to bare hematite. Electrochemical impedance spectroscopy has contributed to shine light on the mechanisms of photocurrent generation, confirming the reduction of recombination pathways as the main contributor to the improved performances of the functionalized photoelectrodes. Our results highlight the importance of the amorphous catalysts' morphology, since dense and electrolyte impermeable layers hinder the pivotal charge compensation processes at the interface. The direct comparison with all-iron and all-nickel catalytic counterparts further confirm that the control over kinetics of both hole transfer and charge recombination, enabled by the adaptive junction, is key for the optimal operation of this kind of semiconductor/catalyst interfaces.

1. INTRODUCTION

Photoelectrochemical water splitting is one of the most pursued strategies aimed at producing hydrogen fuel through the exploitation of abundant and renewable resources, such as water and sunlight.[1] In this sense, most of the reported approaches rely on the use of photoelectrochemical cells (PEC) featuring semiconductor materials, that fulfill the double role of visible light absorbers and photogenerated carriers' separators.[2] In such a set-up, the efficiency of the overall water splitting process is generally hampered by the water oxidation reaction, which is both thermodynamically and kinetically demanding.[3,4] Indeed, an efficient water oxidation catalysis is also central to other important fuel-forming reactions, such as CO_2 reduction,[5,6] as well as to the development of photoelectrochemical cell technology in general. Thus, the development of efficient photoanodes is of paramount importance. Furthermore, in view of a future industrial implementation of this kind of approach, earth-abundant and cheap materials should be preferred. We thus propose novel photoanodes entirely constituted by first-row transition metals, namely iron and nickel. In particular, hematite (α-Fe_2O_3) is the semiconductor of choice, possessing: (i) a small band gap (*ca.* 2.1 eV) which allows for the absorption of a significant portion of the visible light spectrum, resulting in theoretical photocurrent densities up to 12.6 mA/cm^2; (ii) a valence band maximum positioned at more positive potentials with respect to the water oxidation potential; (iii) essentially null toxicity and (iv) good chemical stability in alkaline aqueous media. However, hematite's photoanodic performances are severely limited by the short hole diffusion length (2-10 nm),[7] which contrasts with the optical penetration depth (*ca.* 100 nm for a 500 nm photon wavelength),[8] as well as by the low conductivity of the majority carriers[9] and, to a less extent, by the hole transfer kinetics to the electrolyte.[10] All these features result in extracted photocurrent values far below the theoretical maximum. Anyway, several strategies have been proposed in order to overcome such limitations, including: (i) the rational nanostructuring of the hematite film, aimed at obtaining morphologies with comparable size to that of the hole diffusion length, as, for example, in a vapor phase deposited hematite, which displays 5-10 nm-size particles at the tip of the tree-like aggregates;[11] (ii) the

introduction of substitutional dopant elements in the lattice (such as, but not limited to, Ti(IV),[12–14] Sn(IV),[15] Si(IV),[11] Pt(IV)[16] and Mg(II)[17]), in order to enhance the electrical conductivity; (iii) the functionalization with suitable oxygen evolving catalysts (OECs), able to boost the interfacial kinetics of water oxidation exploiting their ability to collect and store photogenerated holes.[18–24] This latter aspect is still a hotly debated topic in the literature, since some groups have reported on effects different than hole collection (*e.g.* passivation[25] or the enhanced depletion layer width[26,27]) as the main reason for the improved performances of OEC-functionalized hematite electrodes. A further complication to take into account is the type of junction formed between the hematite absorber and the OEC. Recent reports[21,28,29] have detailed the importance of establishing an adaptive rather than a buried junction, which can be achieved with a porous instead of a compact OEC morphology.

In this work, we combine the three abovementioned strategies for the design of a photoanode consisting of Sn-doped thin layer hematite (SnHTL) functionalized with amorphous nickel/iron oxides OECs. Fine-control of the OEC morphology down to the nanometric scale is achieved by employing the pulsed laser deposition (PLD) technique, allowing for the formation of an adaptive junction. The merging of all these features leads to enhanced photoanodic performances when compared to the single-metal oxide counterparts and/or to compact OECs morphology. With respect to recent literature, where other hematite/nickel-iron oxides interfaces are investigated,[30,31] our work reports a systematic approach of comparison between porous or compact catalyst morphology and between the mixed-metal oxide and its single-metal oxide counterparts. An in-depth (photo)electrochemical characterization allows then to identify the key factors dictating the photoanode performance and to gain insights into the photocurrent generation mechanism by the modified interfaces.

2. EXPERIMENTAL METHODS

General procedures. FTO slides were cleaned by 10 min sonication in an Alconox® aqueous solution, followed by 10 min sonication in isopropanol. Quartz and p-Si

substrates were cleaned by 10 min sonication in acetone, followed by rinsing with isopropanol. The electrolytic solutions (either 0.1 M or 1 M KOH) were purified according to literature procedures.[32]

Synthesis of OECs. Ni, Fe and NiFe oxides OECs were synthesized by a PLD method on the following substrates: commercial (Sigma-Aldrich) quartz and p-type Si substrates (for UV-Vis and SEM characterization, respectively), commercial (Sigma-Aldrich) FTO (for Raman spectroscopy and electrochemistry) and on FTO/SnHTL electrodes (for photoelectrochemistry). For single metal oxides, a metallic disk (purity 99.9% for Fe and 99.95% for Ni, Sematrade) was used as the target, while for the mixed oxides the target was a metallic iron disk (99.9%, Sematrade) with a nickel gauze mounted on top (50 mesh woven from 0.05mm diameter Puratronic® wire, 99.99% purity, Alfa-Aesar). PLD was carried out using a KrF excimer laser (Lambda Physik LP 220i) with an operating wavelength of 248 nm, pulse duration of 25 ns, repetition rate of 20 Hz, and laser fluence of 2.0 J/cm^2. The deposition chamber was evacuated up to a base pressure of 10^{-4} Pa, oxygen gas was then backfilled into the chamber through a mass flow controller. Deposition was performed at a constant oxygen pressure of 45 Pa. The distance between the metallic iron target and substrates was set to 5.5 cm and the number of pulses was fixed (2,000 pulses), to ensure that all samples have the same quantity of material. A set of samples on p-Si was produced with 20,000 pulses specifically for SEM cross-section and Energy Dispersive X-ray Spectroscopy (EDXS) analysis. Substrate temperatures were either room temperature or 300°C (DEP). A more detailed description of the PLD apparatus is available elsewhere.[33] Samples deposited at room temperature were then annealed for 2 hours at 300°C (AN) in air in a tubular furnace, with a heating rate of 10 °C/min.

Synthesis of SnHTL. 0.5 mmol (0.135 g) di $FeCl_3$ and 5 µmol (1% doping) of $SnCl_4$ were dissolved in 5 mL of EtOH containing 120 µL di PEG-600 as additive. The resulting solution was spin coated on cleaned FTO slides (600 rpm for 6 s, then 2000 rpm for 20 s). Three spin coating cycles were performed, each one followed by an annealing step at 550°C for 15 min. A final annealing at 800°C was then performed. It is worth noting that a final annealing up to 800°C for 10 min is needed in order to

achieve good photoelectrochemical performances, since further Sn will be incorporated in the hematite structure by partial migration from the FTO substrate, thus enhancing the doping while reducing the grain boundaries and the superficial concentration of hydroxyl- moieties, acting as recombination centers. At the same time, it is important not to exceed in the annealing time at 800°C, since the conductibility of FTO can be severely compromised.

Characterization of the (photo)electrodes. SEM-EDXS analysis was performed using a JEOL JSM-7001F FEG-SEM equipped with an EDXS (Oxford INCA PentaFETx3). Measurements were taken with 20.0 keV electron beam energy and the working distance was maintained between 3 to 8 mm. Surface morphology images were acquired in top-down and tilted mode whereas cross section analysis was performed putting the films on a 90° stub. Raman measurements were performed on a Horiba LabAramis setup equipped with a HeNe 633 nm laser as source and a confocal microscope (100x objective) coupled to a 460 mm-focal length CCD-based spectrograph equipped with a four interchangeable gratings-turret. In the range between 450 nm and 850 nm, the wavenumber accuracy is 1 cm^{-1} with an 1800 l/mm grating. The laser power is 15 mW and the maximum spot size is 5 µm. An accumulation number of 10 and an exposure time of 7 s were employed for all measurements. XPS was performed using a PHI 5000 VersaProbe II equipped with a mono-chromatic Al K_α (1486.6 eV) X-ray source and a hemispherical analyser. Electrical charge compensation was required to perform the XPS analysis. Data analysis was performed using the XPSPeak 4.1 software, using a Shirley-type background and a weighted least-squares fitting of model curves (20% Gaussian, 80% Lorentzian) to the experimental data to obtain peak positions. Atomic force microscopy (AFM) images were collected using a Digital Instruments Nanoscope III scanning probe Microscope (Digital Instruments, CA). The instrument was equipped with a silicon tip (RTESP-300 Bruker) and operated in tapping mode. Surface topographical analysis of raw AFM images was carried out with Nanoscope analysis 1.5 program. UV-Vis absorption spectra were measured in transmission mode with a JASCO V-570 and corrected for the bare FTO background. Photoelectrochemical measurements were carried out on a PGSTAT 30 electrochemical workstation in a

three-electrode configuration, using SCE and Pt wire respectively as the reference and the counter electrode. A LOT-Oriel solar simulator, equipped with an AM1.5G filter, was used as the illumination source, and set to 0.1 W/cm^2 incident irradiance power by means of a Power Meter (Newport 1918-C). J-V curves were recorded at 20 mV/s scan rate in the KOH purified electrolyte. J-V curves under shuttered illumination were acquired by manually chopping the excitation source. Unless otherwise stated, all the potential values are given versus the reversible hydrogen electrode (RHE), through the following equation:

$$E_{RHE} = E_{SCE} + 0.24 + 0.059 \cdot pH$$

Incident Photon to Current Efficiencies (IPCEs) were measured in a three-electrode configuration under the monochromatic illumination generated by an air cooled Luxtel 175 W Xe lamp, coupled to an Applied Photophysics monochromator. The resulting photocurrent, recorded at the selected constant potential, was measured by a PGSTAT 30 potentiostat. Absorbed Photon to Current Efficiencies (APCEs) were calculated from IPCE data by normalizing them for the light harvesting efficiency (LHE) obtained from absorption spectra.

Electrochemical Impedance Spectroscopy (EIS) under illumination, the photoanodes were sampled from 0.92 to 1.32 V at 50 or 100 mV intervals, employing a FRA2.v10 frequency response analyzer controlled by Nova 1.10. A 10 mV amplitude sinusoidal perturbation, whose frequency ranged between 100000 and 0.05 Hz, was used. The EIS data were fitted by means of the equivalent circuit reported in Figure S12a using the ZView software, with typical relative errors lower than 10%.

3. RESULTS AND DISCUSSION

3.1 Structural and Morphological Characterization

Mixed-metal oxide coatings of iron and nickel (NiFe) and their single-metal counterparts (Ni, Fe) are obtained by PLD in oxygen atmosphere from metallic targets. Substrate temperature was either room temperature (RT) or 300°C. The nomenclature selected to indicate samples accounts for the abovementioned different deposition temperature, being DEP the designation for the samples

deposited at 300°C, while AN indicates the samples prepared at room temperature and successively submitted to a 2 h post-annealing step at 300°C. It is worth pointing out that this annealing step is not expected to significantly alter the morphology of the deposited materials, but it only leads to some aggregation of the smaller particles. On the other hand, the post-annealing treatment significantly improves the adhesion on the conductive FTO substrates, which translates in a better long-term stability.[21] Furthermore, the two synthetic routes yielding DEP and AN oxides, have been purposely designed to provide different film morphology, yet the same amount of metal catalyst. This is possible since the oxide morphology, for fixed laser pulse energy, is dictated by the substrate temperature, whereas the quantity of deposited material critically depends on the background gas pressure, which in our case is kept constant.

Figure 1 shows the scanning electron microscopy (SEM) images of all the deposited oxides. It can be clearly seen that, as expected,[21] two different film morphologies are obtained through the two deposition procedures. In all cases, the depositions at RT with subsequent annealing at 300°C resulted in a highly porous and nanostructured oxide layer (see Figure 1, left column). On the other hand, the depositions performed with the substrates heated at 300°C produce a compact morphology, with assembled nanoparticles (see Figure 1, right column). This effect is due to the higher mobility of the particles when they hit the heated substrate, leading to aggregation and the formation of bigger and partially fused particles,[34] as also observed in the previous characterization of both the single-metal oxides.[21,35]

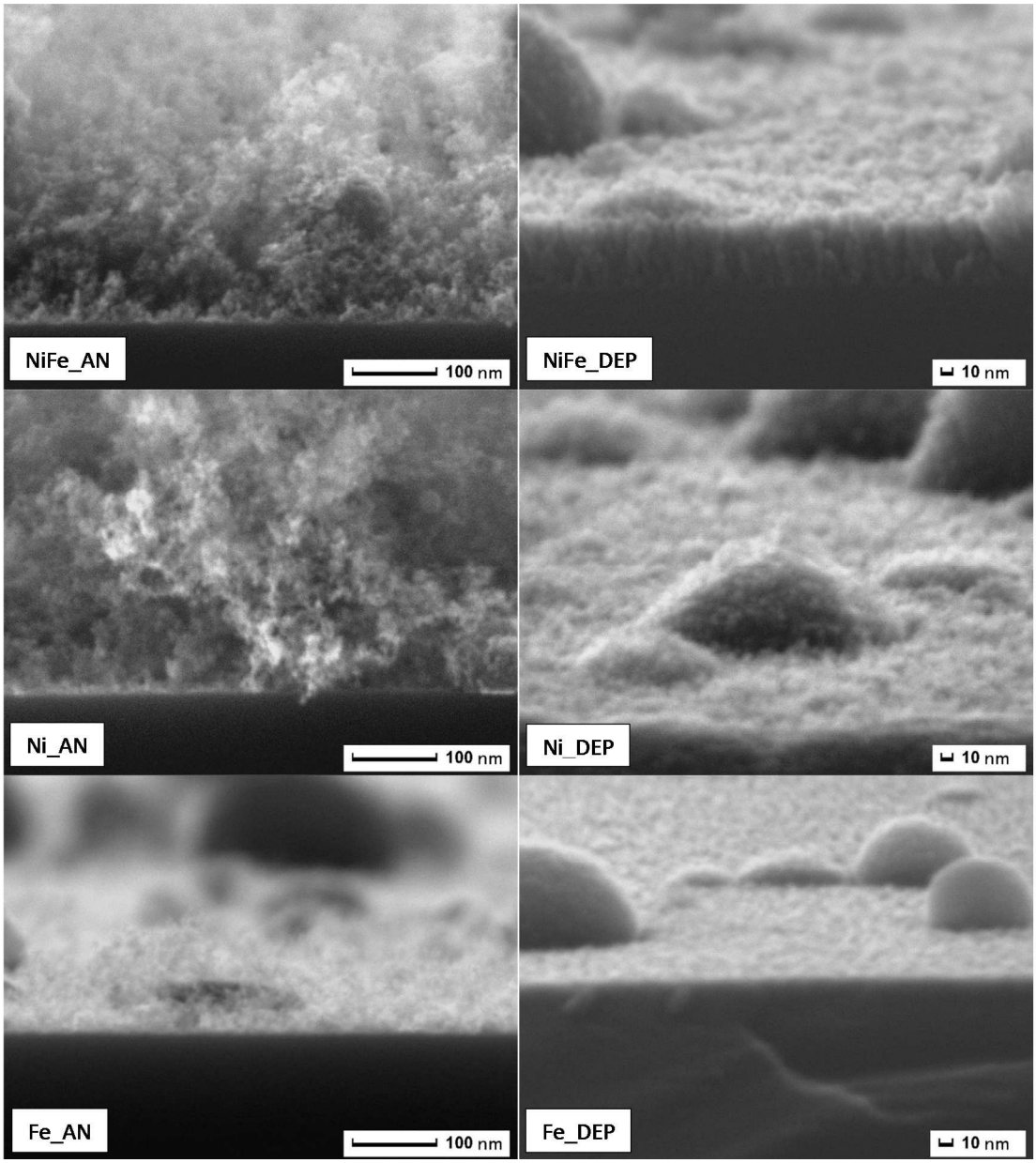

Figure 1. SEM cross-section images of catalyst layers deposited on silicon slides. Thicker layers, produced by 20,000 (20k) laser pulses instead of 2,000 (2k) were analyzed here for better cross-section imaging. First row: NiFe_AN (left) and NiFe_DEP (right). Second row: Ni_AN (left) and Ni_DEP (right). Third row: Fe_AN (left) and Fe_DEP (right).

Further spectroscopic characterization of the thin oxides has been performed by means of micro-Raman analysis, aimed at identifying the amorphous/crystalline nature of the deposited materials. As reported in Figure S1, the Raman spectra of both DEP and AN samples reveal only broad, unresolved features, almost superimposable on those of FTO, thus indicating that the metallic oxides are largely

amorphous in nature. Note that, at least for the more compact morphology, metal-oxide layers of similar thickness but annealed at higher temperatures (>550°C), have been reported to exhibit clear spectral signatures.[36] It is worth noting that the non-crystallinity of these catalytic materials does not jeopardize their activity towards water oxidation, on the contrary, it is expected to enhance it. Several examples of amorphous OECs more active than their crystalline counterparts have been reported so-far.[37–42]

X-ray photoelectron spectroscopy (XPS) has been employed to investigate the chemical composition of the films and the results for NiFe_DEP and NiFe_AN are reported in Figure 2 and summarized in Table 1.

Table 1. XPS data for NiFe_DEP and NiFe_AN, extrapolated from Figure 2.

Sample	B.E. (eV) ± 0.5 eV		Attribution
NiFe_DEP	854.6	Ni 2p 3/2	NiO
	855.7	Ni 2p 3/2	$Ni(OH)_2$ – NiOOH - $NiFe_2O_4$
	861.2	Ni 2p 3/2	$Ni(OH)_2$ – NiOOH
	865.3	Satellite	NiO
	710.3	Fe 2p 3/2	Fe_2O_3 – $NiFe_2O_4$
	712.1	Fe 2p 3/2	$Fe(OH)_3$ – FeOOH
	718.2	Satellite	Fe_2O_3
	723.8	Fe 2p 1/2	Fe_2O_3
	725.6	Fe 2p 1/2	FeOOH
	529.7	O 1s	NiO - Fe_2O_3 – $NiFe_2O_4$
	531.2	O 1s	FeOOH - $Ni(OH)_2$ – NiOOH
NiFe_AN	855.0	Ni 2p 3/2	NiO
	856.0	Ni 2p 3/2	$Ni(OH)_2$ – NiOOH - $NiFe_2O_4$
	861.4	Ni 2p 3/2	$Ni(OH)_2$ – NiOOH
	866.1	Satellite	NiO
	710.5	Fe 2p 3/2	Fe_2O_3 – $NiFe_2O_4$
	712.4	Fe 2p 3/2	$Fe(OH)_3$ - FeOOH
	718.5	Satellite	Fe_2O_3
	723.6	Fe 2p 1/2	Fe_2O_3
	725.5	Fe 2p 1/2	FeOOH
	529.9	O 1s	NiO - Fe_2O_3 – $NiFe_2O_4$
	531.5	O 1s	FeOOH - $Ni(OH)_2$ – NiOOH

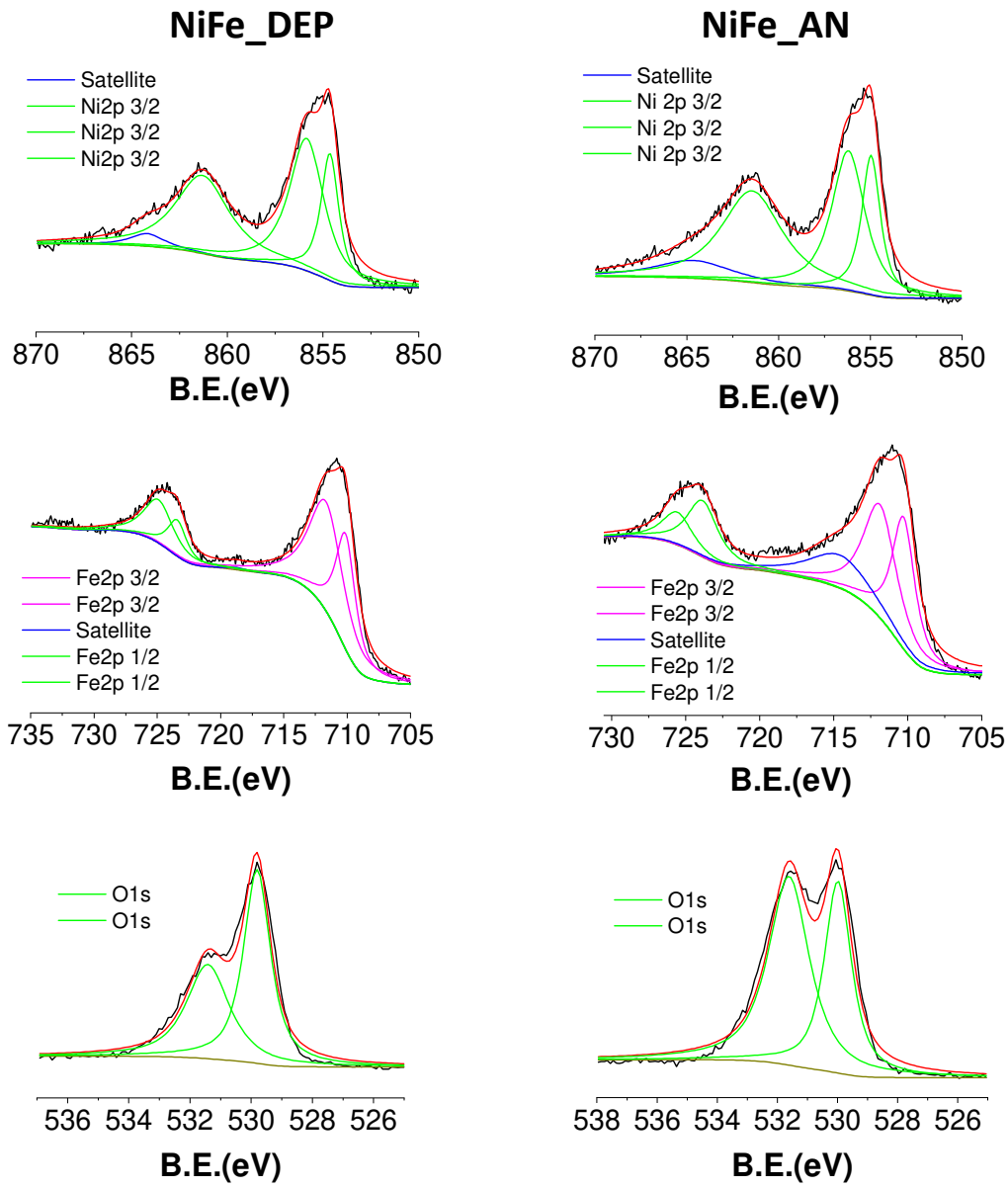

Figure 2. XPS spectra and corresponding fits for NiFe_DEP and NiFe_AN. Raw data is reported as a black line, fitting curves in red and background in gold.

The corresponding analysis for the single-metal oxides are reported in Table S1, while the XPS spectra are collected in figure S2. All the signals can be attributed to Fe^{3+}, Ni^{2+} and O and are compatible with the presence of the single-metal oxides (Fe_2O_3 and NiO),[43-48] their related hydroxide-oxyhydroxide systems ($Ni(OH)_2$ – NiOOH, $Fe(OH)_3$ – FeOOH)[45,48,49-52] and the $NiFe_2O_4$ mixed-metal oxide.[45,49,53,54] The formation of hydroxide-oxyhydroxide species is due to hydroxylation upon exposure to air humidity and is a common feature for metal-oxide surfaces.[55]

Energy-dispersive X-ray spectroscopy (EDXS) analysis (Figure S3) performed on the thicker (20k pulses) layers, confirms the uniform presence of Fe and Ni, with an atomic ratio of 1.5-1.7/1. We thus attribute to NiFe_DEP and NiFe_AN films a stoichiometry of $NiFe_{1.5\text{-}1.7}O_x$.

The UV-Vis spectra of the thin oxide films are reported in Figure S4, confirming their scarce absorbance (< 0.2) and excluding a significant parasitic light absorption when they are used in combination with photoanodes. In all the cases, the porous morphology leads to even lower absorption (< 0.1), with the best transparencies achieved with NiFe_AN and Ni_AN (≤ 0.05 at 300 nm).

3.2. Electrochemical Properties of the Catalytic Layers

The electrochemical activity of the DEP and AN amorphous oxides has been tested in 0.1 M KOH, since these metal oxides are known to be stable in basic pHs.[56] It is worth noting that all the (photo)electrochemical characterizations reported in this work have been performed in a purified "Fe-free" KOH electrolyte. Indeed, as extensively studied by Boettcher and co-workers,[32] even sub-ppm amounts of iron in the electrolytic solution can be incorporated in the nickel-oxide structure, thus forming layered mixed NiFe oxides and, therefore, altering the actual performances of the pure nickel oxide catalysts.

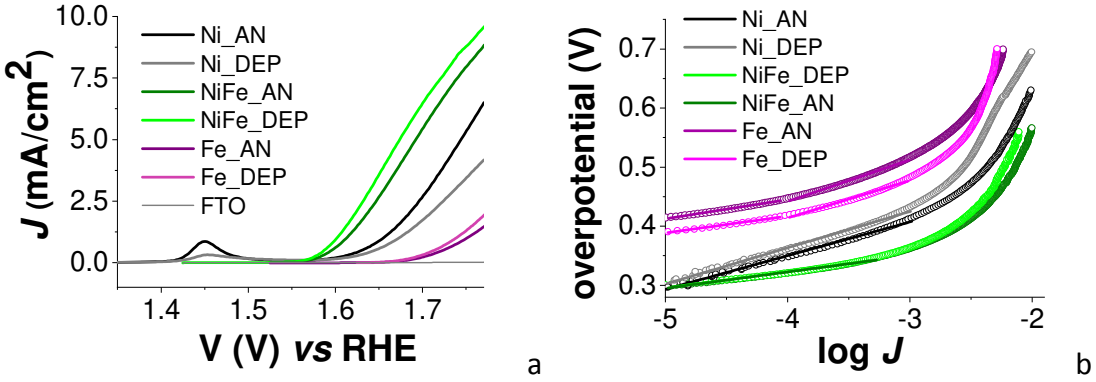

Figure 3. iR-drop compensated J-V curves for the DEP and AN oxides registered in purified 0.1 M KOH (a) and the corresponding Tafel plots (b).

As evidenced by the current density versus potential (J-V) curves reported in Figure 3a, all the catalysts result to be active toward water oxidation, in the order NiFe > Ni > Fe. Furthermore, these experiments evidenced that the electroactivity does not significantly change upon varying the film morphology. Indeed, porous and compact films display pretty much the same onset of the catalytic current (values given at 1 mA/cm^2 and reported in Table 2, together with the corresponding overpotentials). It is worth noting that in the case of the pure nickel oxide catalysts, a pre-wave, corresponding to the oxidation of Ni(II) to Ni(III) has been also observed at potential values of 1.44 V vs RHE.

Table 2. Results of the electrochemical analyses for all the oxides.

OEC	Onset (@1 mA/cm^2), V	Overpotential, η (@1 mA/cm^2), V	Tafel slope (mV/dec)
Ni_AN	1.65	0.42	58
Ni_DEP	1.67	0.44	61
NiFe_AN	1.60	0.37	28
NiFe_DEP	1.60	0.37	27
Fe_AN	1.75	0.52	32-70
Fe_DEP	1.73	0.50	28-63

The Tafel analysis further confirms that the mixed NiFe catalysts outperform the two pure counterparts (Figure 3b). While a linear trend has been observed over two current decades for both NiFe- and Ni-based catalysts, in the case of Fe-oxides the Tafel characteristics are less linear, and could better be fitted with a polynomial function. This behavior can be reasonably ascribed to a more significant variation of the surface coverage of the adsorbed intermediates of water oxidation as a function of the applied potential. Furthermore, for all the catalysts, a saturation region starts to be evident at η > 0.4 V, where the current tends to become essentially

independent on the applied bias, suggesting that in these conditions all anodes tend to reach a kinetic regime dominated by the chemical desorption of molecular O_2 (Volmer-Tafel mechanism).[57]

3.3 Photoelectrochemical Properties of functionalized hematite

Given their good electrochemical performances, all the thin film catalysts have been deposited on the Sn-doped hematite photoanodes (SnHTL). These electrodes have been prepared using a new and straightforward synthetic procedure involving the spin-coating and successive annealing of suitable precursors on FTO electrodes (see the Supporting Information for further details). This synthesis yields thin layer hematite photoanodes displaying a quite uniform coverage of nanoparticles, homogeneously distributed both in shape and size, with an average diameter of *ca.* 50 nm, as evidenced by means of atomic force microscopy (Figure S5). The thin films showed 0.7 maximum absorbance at 400 nm, tailing up to 590 nm, in agreement with the band gap energy (2.1 eV theoretical value *versus* 2.3 eV calculated by the experimental Tauc plot, see Figure S6). From the absorption spectrum, the layer thickness can be estimated to be *ca.* 70 nm (given $2.3 \cdot 10^5$ cm^{-1} the absorption coefficient of hematite at 400 nm[8]). This value has been further confirmed by SEM analysis (Figure S7). This layer thickness has been shown to be a good compromise between light absorption and charge collection, since the photoelectrochemical performances of thick hematite films are strongly limited by the short minority carrier diffusion length.[13] Indeed, our SnHTL electrodes show photocurrent values up to 0.55 mA/cm^2 at 1.67 V (the onset of the dark current) when tested under 0.1 W/cm^2 AM1.5G solar simulated irradiation in purified 0.1 M KOH (Figure 4, orange curve).

The photoelectrochemical performances of this photoanodic material can be further boosted by the introduction of the transparent catalytic films deposited by PLD. Figure 4a reports the photoelectrochemical performance of the SnHTL electrodes functionalized with the two kinds of mixed NiFe oxides in purified 0.1 M KOH, compared to the bare hematite. The samples have been illuminated through the

electrolyte/hematite interface (front irradiation), as opposed to illumination through the electron collector (FTO, back illumination).

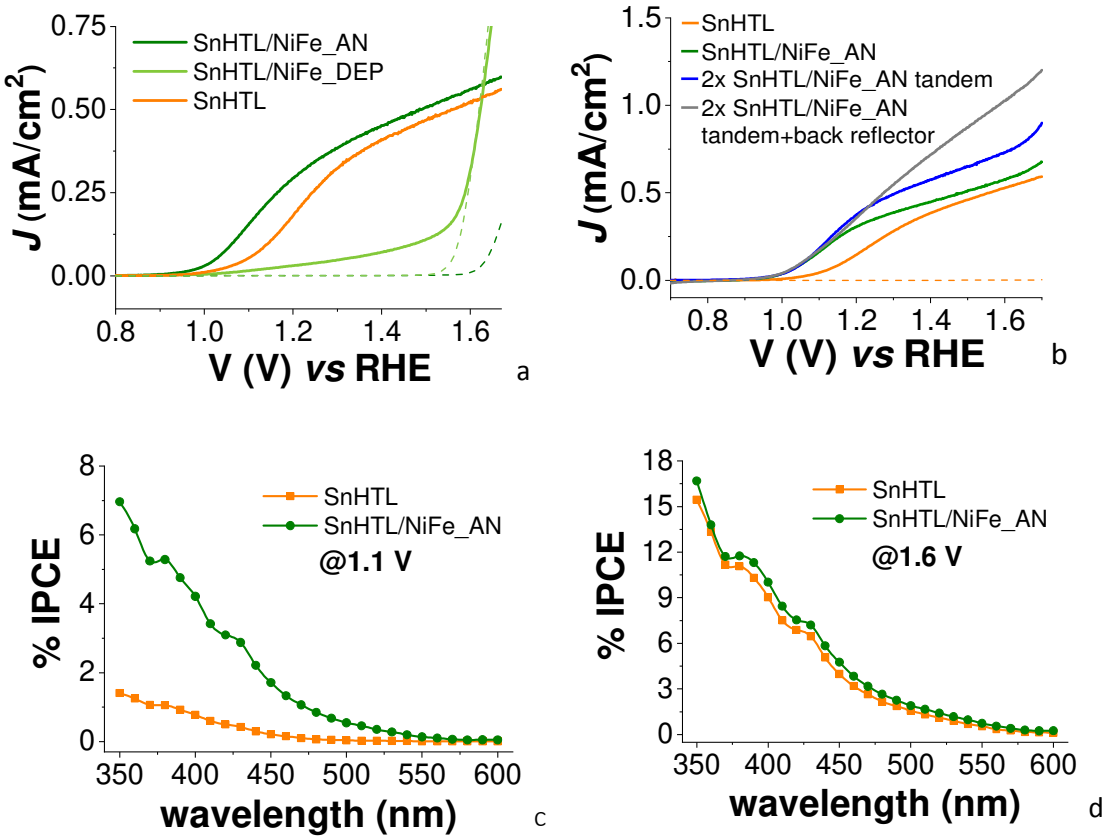

Figure 4. a) J-V curves of SnHTL photoanodes, before (orange) and after the functionalization with NiFe_AN (dark green) and NiFe_DEP (light green), recorded in purified 0.1 M KOH under 1 sun illumination (0.1 W/cm^2 AM1.5G). The corresponding dark J-V curves are reported as dashed lines; b) J-V curves of 2 SnHTL/NiFe_AN photoanodes in tandem configuration, with (gray) and without (blue) an Al back reflector. The J-V curve of the single SnHTL (orange) and SnHTL/NiFe_AN (dark green) are also reported for sake of comparison, together with the dark curve for SnHTL (orange dashed line); c-d) Incident photon to current conversion efficiency (IPCE) curves for SnHTL (orange) and SnHTL/NiFe_AN (dark green) recorded in purified 0.1 M KOH (pH 13.3) under 1.1 V (c) and 1.6 V (d) vs RHE applied bias; front illumination.

The results evidence the striking differences between compact and porous catalysts. It can be clearly seen that when the interface is functionalized with the NiFe_AN, *i.e.*

the porous catalyst, we observe a 0.1 V shift in the photocurrent onset with respect to the bare hematite, as well as an increase in the total photocurrent (up to 0.6 mA/cm^2 at 1.65 V). It is also interesting to observe that the J-V curves obtained by irradiating through the transparent electron collector (FTO side) are slightly lower than those obtained by excitation through the electrolyte (Figure S8), probably due to a partial absorption of < 380 nm light by the FTO. The photoaction spectra (collected under monochromatic illumination and 1.1 V applied bias, Figure 4c) further confirm the improved performances upon functionalization, being the incident photon to current conversion efficiency (IPCE) of the SnHTL/NiFe_AN electrode *ca.* three times higher than that of the bare SnHTL in the whole wavelength region explored (7% maximum IPCE at 350 nm, corresponding to 10% APCE, absorbed photon to current conversion efficiency, in Figure S9a). At the photocurrent plateau (*i.e.* under 1.6 V applied bias), SnHTL and SnHTL/NiFe_AN electrodes reach 15% and 17% IPCE values, corresponding to 20% and 24% APCE values respectively (Figures 4d and S9b). The presence of the OEC thus offers a major gain at lower overpotentials, corresponding to the activation region of the J-V curve, where recombination is more important. In addition, the good transparency of the catalyst allows for the front side illumination of photoanode, which enables the assembly of tandem PEC configuration, where photons transmitted through the first electrode can be absorbed by a second cell or photoelectrode. This latter set-up has been realized by the parallel connection of a stack of two SnHTL/NiFe_AN electrodes delivering a maximum photocurrent of 0.79 mA/cm^2 at 1.65 V, which could be further enhanced up to 1.1 mA/cm^2 by introducing an Al back reflector (Figure 4b).

Conversely to the functionalization with NiFe_AN, when NiFe_DEP is deposited on top of hematite, the photoresponse of the resulting photoanode results almost completely suppressed (light green curve in Figure 4a). These observations are in line with our previous report on pure iron oxide amorphous catalysts,[21] yielding a so-called adaptive junction when coupled with hematite semiconductors.[28] Briefly, unlike compact catalysts, porous amorphous catalysts display accessible electronic states (in which the photogenerated holes can be trapped and accumulated), resulting in the decoupling of the quasi-Fermi level of the semiconductor from that

of the catalyst/electrolyte junction.[23,28] Furthermore their good solvent permeability enables ion migration, which in turns leads to a better charge compensation at the interface. On the other hand, compact and dense catalysts yield buried junctions with the semiconductor, thus severely hampering the hole transfer to the electrolyte and jeopardizing the charge separation and photovoltage generation of the functionalized electrodes.[28]

After the rationalization of the photoanodic behavior of SnHTL/NiFe interfaces, we extended the study to the pure Ni- and Fe-oxide based counterparts. Figure S10 reports the performances of SnHTL functionalized with the pure nickel oxides, evidencing again the almost complete suppression of the photoanodic response of hematite in the presence of compact Ni_DEP catalyst (compare gray and orange curves). Furthermore, the SnHTL/Ni_DEP electrode results essentially insensitive to light, as evidenced by the almost perfect matching of the J-V curves collected in the dark or under illumination (gray traces). Thus, in this latter case, given the insulating properties of hematite in the dark, the electrochemical response is most probably due to just the Ni_DEP particles in electrical contact with the underlying FTO, (as evidenced by the presence of the Ni(II)/Ni(III) wave in the dark) possibly causing shorting when the photoanode operates under illumination.[58] On the other hand, the functionalization with porous Ni_AN does not yield the expected improved performances (compare black and orange curves), yet not completely suppressing the photoresponse. This behavior can be ascribed to the lower intrinsic activity of pure Ni oxides with respect to the mixed NiFe (as reported in the literature[40,56] and consistent with the Tafel slopes in Table 2), resulting in a photoanodic assembly limited by the charge transfer to the electrolyte (vide infra and Figure 6a). Anyway, a direct evidence of the formation of the two different kinds of junctions upon functionalization of SnHTL with the two different nickel oxide morphologies is indeed given by the *ca.* 0.45 V cathodic shift of the Ni(II)/Ni(III) wave for Ni_AN with respect to Ni_DEP, even if this value results lower than that of unmodified SnHTL (0.7 V, estimated for the onset of the corresponding J-V curves in the dark and under illumination), as a probable consequence of charge recombination. Anyway, the photovoltage cannot be exploited in the case of Ni_DEP compact layer, since the

resulting junction experiences the pinning of the quasi-Fermi level of hematite to that of the catalyst.

The photoanodic performances obtained upon functionalization of SnHTL with pure Fe oxides are reported in Figure S11. We have limited the study to SnHTL/Fe_AN electrodes, since the functionalization of hematite with Fe_DEP has been already proven to be scarcely effective.[21] In spite of our expectations, the presence of the porous Fe_AN leads to a decrease in the total photocurrent (0.45 *vs* 0.55 mA/cm^2 at 1.67 V), while the onset remains the same. We can rationalize this evidence by invoking subtle differences in the surface of the SnHTL electrodes with respect to that of the undoped hematite thin layers (HTL) used in our previous work,[21] which has possibly led to less uniform PLD deposition of the catalytic Fe layers. Indeed, due to the well-known poor electrical conductivity of amorphous iron oxides,[56] the possible presence of regions with thicker agglomerates of catalyst can introduce a voltage drop, partially preventing the access to Fe centers more distant from the substrate, thus hindering the water oxidation kinetics. Recombination rate is also higher for SnHTL/Fe_AN photoanodes when compared to bare SnHTL, as it will be discussed later in the manuscript (Figure 6b).

3.4 Electrochemical Impedance Spectroscopy of the Photoanodes

In order to gain further insights on the interfacial processes associated with the photoelectrochemical performances of the functionalized photoanodes, we have performed electrochemical impedance spectroscopy (EIS) experiments on the SnHTL photoanodes functionalized with the three kinds of porous catalysts.

The complex plane Nyquist plots, recorded under different applied biases (in the steepest region of the J-V curves) are reported in Figure S12 along with the corresponding fittings and the selected circuital model, a nested mesh generally used to describe functionalized hematite interfaces.[20,21] All the photoanodes share similar impedance features, consisting of two semicircles. The high-frequency arc is in all cases attributed to the charge transport through the space charge (SC) layer of the semiconductor, characterized by the CPE_{SC} constant phase element (*i.e.* a non-ideal capacitance, [note 1]) and the R_{SC} resistance (see Figure S12a). Ideally, the low-

frequency semicircle is associated to the charge transfer (CT) from the catalyst states to the electrolyte as far as the functionalized electrodes are concerned, whereas it is related to the transfer of hole trapped in hematite surface states in the case of the bare photoanode. Intermediate situations where the CT occurs from both the catalyst and the hematite surface exposed to the electrolyte could however exist, depending on the electrode regime of operation. For sake of simplicity, the capacitance and resistance values associated to these processes are indicated as CPE_{CT} and R_{CT} without further distinction (Figure S12a).

Figure S13 shows the inverse of the differential resistance (dI/dV, calculated from the I-V curves) *versus* the applied potential (gray curves), compared to R_{SC}^{-1}, R_{CT}^{-1} and R_{tot}^{-1} values (being $R_{tot} = R_s + R_{SC} + R_{CT}$ the total resistance and R_s the serial resistance associated to the cell geometry). It can be clearly seen that R_{tot}^{-1} nicely correlates with the dI/dV curve in all cases, confirming that the selected circuital model properly describes the active elements involved in photocurrent generation, thus validating the resistance and capacitance values extracted from the fit. At the same time, we can establish that at $V < 1.12$ V the major resistive contribution to the photocurrent generation is given by R_{CT}, the resistance associated with the charge transfer to the electrolyte, which follows the same trend of the dI/dV curve in the explored potential range. The J-V curves are instead dominated by the charge transport through the space charge (R_{SC}) at higher potentials (> 1.12 V), as previously reported also by the Hamman group.[20]

It is also worth noting that for SnHTL, the C_{CT} shows a bell shaped dependence on the applied bias (Figure S14, orange curve), typical of the photogenerated holes trapping in surface states,[20,21,59] progressively emptied by the anodic potential scan. These trapped holes on hematite surface are generally deemed as highly valent iron-oxo species, the key reactive intermediates for oxygen evolution.[60] Upon functionalization with NiFe_AN, the C_{CT} maintains the bell-shaped trend, with *ca.* 10 times higher values with respect to bare SnHTL (see Figure S14, green *vs* orange curve). Furthermore, the C_{CT} maximum results cathodically shifted by 0.25 V, speaking in favor of a direct involvement of the catalyst in the storage of the photoproduced charges. It is also worth noting that the position of the C_{CT} maximum

(0.97 V) almost coincides with the minimum of the resistance of charge transfer to the electrolyte, R_{CT} (at 1.07 V), as better evidenced in Figure 5. Furthermore, these values are also in agreement with the inflection point of the J-V curve for SnHTL/NiFe_AN (dark green line in Figure 4a), thus clearly indicating that the hole transfer step leading to water oxidation takes place predominantly from surface trapped holes, most likely localized on electronic states of the catalyst.

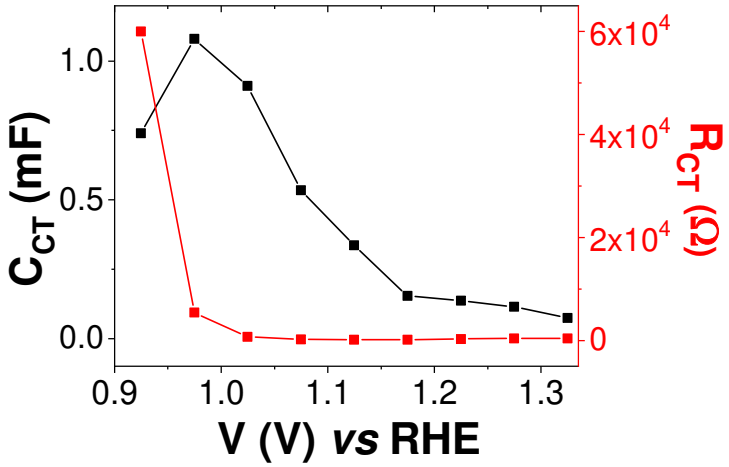

Figure 5. Correlation between C_{CT} and R_{CT} for SnHTL/NiFe_AN photoanodes as a function of the applied bias. The data were extracted from EIS experiments recorded in purified 0.1 M KOH under 1 sun illumination (0.1 W/cm^2 AM1.5G).

From the EIS data, we could also determine the photoelectrochemical water oxidation efficiency (η_{WO}), using the approach reported by Peter *et al.*,[61] and successively implemented by Mendes *et al*.[62] This parameter accounts for the interfacial performances of hematite under illumination, essentially depending on: (i) the kinetics of water oxidation, ultimately ascribable to the reaction between surface trapped holes and surface bound water, and characterized by the charge transfer rate constant to the electrolyte, k_{CT} (note that as far as the functionalized photoanodes are concerned, k_{CT} is associated to the charge transfer from the catalyst states to the electrolyte); (ii) the e^-/h^+ recombination rate (k_{REC}) at the surface of the hematite electrode, which depends on the applied bias, and (as far as the hole concentration is concerned) on the excitation intensity;[61] (iii) the charge

recombination in the bulk of the film, which is neglected in this approach, being almost independent on surface modifications.

Both k_{CT} and k_{REC} can be extracted from the fit of EIS data. By considering the interfacial charge transfer arc, k_{CT} can be obtained using:[63]

$$k_{CT} = (R_{CT} \cdot C_{CT})^{-1}$$

where C_{CT} is the equivalent capacitance calculated as in note 1.

At high applied bias, k_{REC} can instead be obtained by the following simplified equation, where R_{SC} is the charge transport resistance through the space charge:[64]

$$k_{REC} \cong \frac{k_{CT} \cdot R_{CT}}{R_{SC}} \quad ,$$

while the photoelectrochemical water oxidation efficiency (η_{WO}) for the photogenerated charges able to cope recombination and reach the interface is actually a balance between the two rate constants, and can be expressed as follows:

$$\eta_{WO} = \frac{k_{CT}}{k_{CT} + k_{REC}} \ \% \ .$$

The dependence from the applied bias of the calculated η_{WO} is reported in Figure 6c. The results reflect the J-V trend shown in Figure S12b for all the tested photoanodes, further confirming the improved performances (up to 80% WO efficiency) of the hematite thin layers modified with the porous mixed NiFe oxide, the only one able to yield a functional junction when coupled with the semiconductor. Similar efficiencies have been reported by Mendes *et al.* investigating mixed Ru/Ir oxide modified hematite.[62] From the analysis of the rate constants (Figures 6a-b), we can also ascribe this improvement to a reduced recombination (k_{REC} more than one order of magnitude lower for SnHTL/NiFe_AN with respect to bare SnHTL), rather than to an increased charge transfer rate (similar k_{CT} values are found for both photoanodes when V > 1.05 V). The k_{CT} trend for SnHTL/NiFe_AN undergoing a net increase between 0.9 and 1.1 V is apparently unique to such interface and is most likely due to the scarce electrical conductivity of the mixed oxide under relatively low biases. It is indeed well-known that the conductivity of iron-nickel oxides sharply increases

upon oxidation of the Ni(II) centers, which occurs at comparatively lower voltages compared to Fe(III).[23]

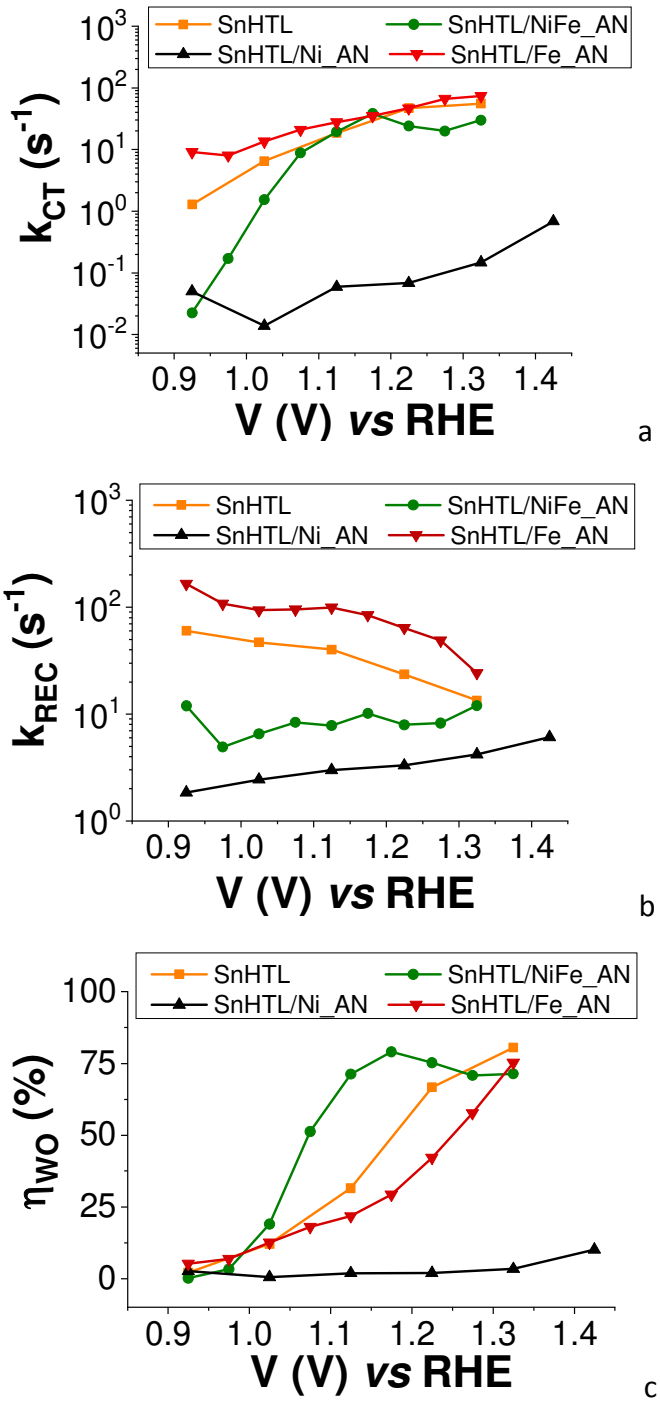

Figure 6. a-c) Rate constants associated to charge transfer (k_{CT}, in a) and recombination (k_{REC}, in b) and water oxidation efficiency (η_{WO}, in c) for SnHTL (orange squares), SnHTL/NiFe_AN (green circles), SnHTL/Ni_AN (black triangles) and SnHTL/Fe_AN (wine reverted triangles). Data extracted from EIS experiments recorded in purified 0.1 M KOH under 1 sun

illumination (0.1 W/cm^2 AM1.5G).

It is also interesting to observe that the reduced recombination with the NiFe oxides provides a clear advantage of the NiFe oxides over the other catalysts presented in this work, despite the fact that, at least up to 1.1 V, the charge transfer rate constant is lower than the other species. Thanks to the reduced recombination, SnHTL/NiFe_AN exhibits, already at 1 V, an interfacial efficiency η_{WO} comparable to that of SnHTL/Fe_AN, which has the best charge transfer properties within the explored series. As the anodic bias increases, SnHTL/NiFe_AN gains the superiority, reaching a maximum η_{WO} value at 1.15 V. The reduced recombination can be probably ascribed to passivation of surface defects, which act as recombination centers in hematite, or to a beneficial heterointerfacial effect, like the one observed with Co-Pi,[65,66] resulting in an increase of the band bending in the space charge region, thus favoring charge separation. However, no evidence of catalytic effect in terms of increased charge transfer rate to the electrolyte was reported in the case of Co-Pi. The fact that SnHTL/Ni_AN displays the lowest recombination rate constant corroborates the formation of heterointerfacial effects useful to retard recombination when Ni oxides are deposited on hematite. Reasonably, in the case of Fe_AN the heterointerface may not form since, basically, two materials with the same type of chemistry are coupled together. As a result, SnHTL/Fe_AN is limited by the highest recombination rate (Figure 6b), while in the case of SnHTL/Ni_AN the main limitation turns out to be the slower rate of charge transfer to the electrolyte (Figure 6a).

CONCLUSIONS

Efficient water oxidation catalysts based on earth-abundant, first-row transition metal oxides (Ni, Fe and mixed NiFe amorphous oxides) have been successfully deposited onto FTO by means of Pulsed Laser Deposition (PLD).

PLD has been proven to be a very versatile route to tune the nanometric morphology of highly transparent catalytic films, which could be obtained by varying

the deposition temperature or the post-annealing parameters, allowing thus for a systematic investigation of the properties of the resulting functional materials in electrochemical and photoelectrochemical cells for water splitting.

Among the explored cases, the most notable improvement in the photoelectrochemical performances of Sn-doped hematite thin films (both in terms of onset shift and total photocurrent) was achieved with the porous mixed oxide (NiFe_AN) overlayer, which incorporates heterointerfacial effects instrumental in retarding recombination and good interfacial charge transfer properties. The combination of these two factors translates in a water oxidation efficiency of ca. 75% at V < 1.2 V vs RHE. We found that the porous morphology of the catalytic layers generally allows for the formation of adaptive junctions, in which the photogenerated holes are efficiently stored within the electronic states of the catalyst and the charge buildup in the catalyst is easily compensated *via* ion migration from the electrolyte, yielding larger charge separation efficiencies at a correspondingly lower bias. On the other hand, compact electrocatalytic layers hamper the hole transfer to the electrolyte, and severely reduce the resulting photocurrent regardless of their response in pure electrochemical conditions. These results are paradigmatic of a common situation in this field, when, upon functionalization of the photoelectrode with a given electrocatalyst, good electrocatalytic performances do not necessarily translate into good photoelectrochemical ones.

Future experiments will be thus aimed at further investigating the optimal composition of the porous catalysts, as well as their interfacial properties when coupled with improved hematite photoanodes, and to other n-type semiconductors suffering from fast recombination/slow water oxidation kinetics, in order to optimize their energy conversion performance. To this end, fabrication methods such as PLD, capable of offering a fine and reproducible control over catalyst stoichiometry and morphology, will be playing a major role.

[note 1] The equivalent capacitance (C) can be obtained from the CPE admittance and n extracted from the fit according to:

$$C = CPE \cdot (\omega)^{n-1}$$

where ω is the angular frequency corresponding to the largest imaginary component of the charge transfer arc and n is the CPE exponent ($0.8 \leq n \leq 1$).

ASSOCIATED CONTENT

The Supporting Information is available free of charge.

Raman spectra of NiFe_DEP and NiFe_AN; XPS analysis and spectra for Ni_DEP, Ni_AN, Fe_DEP and Fe_AN catalysts; EDXS analysis for NiFe_DEP and NiFe_AN; UV-Vis spectra of the OECs deposited on FTO; AFM and SEM images of SnHTL; UV-Vis spectrum of SnHTL and Tauc plot; J-V curves of SnHTL and SnHTL/NiFe_AN upon changing the direction illumination; APCE spectra of SnHTL and SnHTL/NiFe_AN; J-V curves of SnHTL/Ni_AN, SnHTL/Ni_DEP and SnHTL/Fe_AN; Nyquist plots for SnHTL, SnHTL/NiFe_AN, SnHTL/Ni_AN and SnHTL/Fe_AN; Applied bias dependence of the resistance and capacitance values.

ACKNOWLEDGMENTS

The project leading to this application has received funding from the European Union's Horizon 2020 research and innovation programme under the Marie Skłodowska-Curie Grant Agreement No 705723. Project ERICSOL of the University of Trento is also acknowledged for financial support.

References

(1) Lewis, N. S. Research Opportunities to Advance Solar Energy Utilization. *Science (80).* **2016**, *351* (6271), aad1920.

(2) Walter, M. G.; Warren, E. L.; McKone, J. R.; Boettcher, S. W.; Mi, Q.; Santori, E. A.; Lewis, N. S. Solar Water Splitting Cells. *Chem. Rev.* **2010**, *110* (11), 6446–6473.

(3) Ruttinger, W.; Dismukes, G. C. Synthetic Water-Oxidation Catalysts for Artificial Photosynthetic Water Oxidation. *Chem. Rev.* **1997**, *97* (1), 1–24.

(4) McCrory, C. C. L.; Jung, S.; Peters, J. C.; Jaramillo, T. F. Benchmarking Heterogeneous Electrocatalysts for the Oxygen Evolution Reaction. *J. Am. Chem. Soc.* **2013**, *135* (45), 16977–16987.

(5) Habisreutinger, S. N.; Schmidt-Mende, L.; Stolarczyk, J. K. Photocatalytic Reduction of CO2 on TiO2 and Other Semiconductors. *Angew. Chemie - Int. Ed.* **2013**, *52* (29), 7372–7408.

(6) Tu, W.; Zhou, Y.; Zou, Z. Photocatalytic Conversion of CO2 into Renewable Hydrocarbon Fuels: State-of-the-Art Accomplishment, Challenges, and Prospects. *Advanced Materials* **2014**, *26* (27), 4607-4626.

(7) Sivula, K.; Le Formal, F.; Grätzel, M. Solar Water Splitting: Progress Using Hematite (α-Fe2O3) Photoelectrodes. *ChemSusChem* **2011**, *4* (4), 432–449.

(8) Marusak, L. A.; Messier, R.; White, W. B. Optical Absorption Spectrum of Hematite, α-Fe2O3 near IR to UV. *J. Phys. Chem. Solids* **1980**, *41* (9), 981–984.

(9) Horowitz, G. Capacitance-Voltage Measurements and Flat-Band Potential Determination on Zr-Doped α-Fe2O3 Single-Crystal Electrodes. *J. Electroanal. Chem. Interfacial Electrochem.* **1983**, *159* (2), 421–436.

(10) Le Formal, F.; Pastor, E.; Tilley, S. D.; Mesa, C. A.; Pendlebury, S. R.; Grätzel, M.; Durrant, J. R. Rate Law Analysis of Water Oxidation on a Hematite Surface. *J. Am. Chem. Soc.* **2015**, *137* (20), 6629–6637.

(11) Warren, S. C.; Voïtchovsky, K.; Dotan, H.; Leroy, C. M.; Cornuz, M.; Stellacci, F.; Hébert, C.; Rothschild, A.; Grätzel, M. Identifying Champion Nanostructures for Solar Water-Splitting. *Nat. Mater.* **2013**, *12*, 842-849.

(12) Monllor-Satoca, D.; Bärtsch, M.; Fàbrega, C.; Genç, A.; Reinhard, S.; Andreu, T.; Arbiol, J.; Niederberger, M.; Morante, J. R. What Do You Do, Titanium? Insight into the Role of Titanium Oxide as a Water Oxidation Promoter in Hematite-Based Photoanodes. *Energy Environ. Sci.* **2015**, *8* (11), 3242–3254.

(13) Rioult, M.; Magnan, H.; Stanescu, D.; Barbier, A. Single Crystalline Hematite Films for Solar Water Splitting: Ti-Doping and Thickness Effects. *J. Phys. Chem. C* **2014**, *118* (6), 3007–3014.

(14) Dalle Carbonare, N.; Boaretto, R.; Caramori, S.; Argazzi, R.; Dal Colle, M.; Pasquini, L.; Bertoncello, R.; Marelli, M.; Evangelisti, C.; Bignozzi, C.A. Photoelectrochemical Behavior of Electrophoretically Deposited Hematite Thin Films Modified with Ti(IV). *Molecules* **2016**, 21 (7), 942.

(15) Bohn, C. D.; Agrawal, A. K.; Walter, E. C.; Vaudin, M. D.; Herzing, A. A.; Haney, P. M.; Talin, A. A.; Szalai, V. A. Effect of Tin Doping on α-Fe2O3photoanodes for Water Splitting. *J. Phys. Chem. C* **2012**, *116* (29), 15290–15296.

(16) Kim, J. Y.; Magesh, G.; Youn, D. H.; Jang, J. W.; Kubota, J.; Domen, K.; Lee, J. S. Single-Crystalline, Wormlike Hematite Photoanodes for Efficient Solar Water Splitting. *Sci. Rep.* **2013**, *3*, 2681.

(17) Lin, Y.; Xu, Y.; Mayer, M. T.; Simpson, Z. I.; McMahon, G.; Zhou, S.; Wang, D. Growth of P-Type Hematite by Atomic Layer Deposition and Its Utilization for Improved Solar Water Splitting. *J. Am. Chem. Soc.* **2012**, *134* (12), 5508–5511.

(18) Tilley, S. D.; Cornuz, M.; Sivula, K.; Grätzel, M. Light-Induced Water Splitting with Hematite: Improved Nanostructure and Iridium Oxide Catalysis. *Angew. Chemie Int. Ed.* **2010**, *49* (36), 6405–6408.

(19) Zhong, D. K.; Gamelin, D. R. Photoelectrochemical Water Oxidation by Cobalt Catalyst ("Co−Pi")/α-Fe2O3 Composite Photoanodes: Oxygen Evolution and Resolution of a Kinetic Bottleneck. *J. Am. Chem. Soc.* **2010**, *132* (12), 4202–4207.

(20) Klahr, B.; Gimenez, S.; Fabregat-Santiago, F.; Hamann, T.; Bisquert, J. Water Oxidation at Hematite Photoelectrodes: The Role of Surface States. *J. Am. Chem. Soc.* **2012**, *134* (9), 4294–4302.

(21) Orlandi, M.; Dalle Carbonare, N.; Caramori, S.; Bignozzi, C. A.; Berardi, S.; Mazzi, A.; El Koura, Z.; Bazzanella, N.; Patel, N.; Miotello, A. Porous versus Compact Nanosized Fe(III)-Based Water Oxidation Catalyst for Photoanodes Functionalization. *ACS Appl. Mater. Interfaces* **2016**, *8* (31), 20003–20011.

(22) Young, K. M. H.; Hamann, T. W. Enhanced Photocatalytic Water Oxidation Efficiency with Ni(OH)2 catalysts Deposited on α-Fe2O3 via ALD. *Chem. Commun.* **2014**, *50* (63), 8727–8730.

(23) Qiu, J.; Hajibabaei, H.; Nellist, M. R.; Laskowski, F. A. L.; Hamann, T. W.; Boettcher, S. W. Direct in Situ Measurement of Charge Transfer Processes During Photoelectrochemical Water Oxidation on Catalyzed Hematite. *ACS Cent. Sci.* **2017**, *3* (9), 1015–1025.

(24) Ho-Kimura, S.; Williamson, B. A. D.; Sathasivam, S.; Moniz, S. J. A.; He, G.; Luo, W.; Scanlon, D. O.; Tang, J.; Parkin, I. P. Origin of High-Efficiency Photoelectrochemical Water Splitting on Hematite/Functional Nanohybrid Metal Oxide Overlayer Photoanode after a Low Temperature Inert Gas Annealing Treatment. *ACS Omega* **2019**, *4* (1), 1449–1459.

(25) Thorne, J. E.; Jang, J.-W.; Liu, E. Y.; Wang, D. Understanding the Origin of Photoelectrode Performance Enhancement by Probing

Surface Kinetics. *Chem. Sci.* **2016**, *7* (5), 3347–3354.

(26) Barroso, M.; Mesa, C. A.; Pendlebury, S. R.; Cowan, A. J.; Hisatomi, T.; Sivula, K.; Grätzel, M.; Klug, D. R.; Durrant, J. R. Dynamics of Photogenerated Holes in Surface Modified α-Fe2O3 Photoanodes for Solar Water Splitting. *Proc. Natl. Acad. Sci.* **2012**, *109* (39), 15640 LP – 15645.

(27) Barroso, M.; Cowan, A. J.; Pendlebury, S. R.; Grätzel, M.; Klug, D. R.; Durrant, J. R. The Role of Cobalt Phosphate in Enhancing the Photocatalytic Activity of α-Fe2O3 toward Water Oxidation. *J. Am. Chem. Soc.* **2011**, *133* (38), 14868–14871.

(28) Lin, F.; Boettcher, S. W. Adaptive Semiconductor/Electrocatalyst Junctions in Water-Splitting Photoanodes. *Nat Mater* **2014**, *13* (1), 81–86.

(29) Laskowski, F. A. L.; Nellist, M. R.; Qiu, J.; Boettcher, S. W. Metal Oxide/(Oxy)Hydroxide Overlayers as Hole Collectors and Oxygen-Evolution Catalysts on Water-Splitting Photoanodes. *J. Am. Chem. Soc.* **2019**, *141* (4), 1394–1405.

(30) Zhu, Y.; Zhao, X.; Li, J.; Zhang, H.; Chen, S.; Han, W.; Yang, D. Surface modification of hematite photoanode by NiFe layered double hydroxide for boosting photoelectrocatalytic water oxidation *J. Alloys Compounds* **2018**, *764*, 341-346.

(31) Park, Y. B.; Kim, J. H.; Jang, Y. J.; Lee, J. H.; Lee, M. H.; Lee, B. J.; Youn, D. H.; Lee, J. S. *ChemCatChem* **2019**, *11*, 443-448.

(32) Trotochaud, L.; Young, S. L.; Ranney, J. K.; Boettcher, S. W. Nickel-Iron Oxyhydroxide Oxygen-Evolution Electrocatalysts: The Role of Intentional and Incidental Iron Incorporation. *J. Am. Chem. Soc.* **2014**, *136* (18), 6744–6753.

(33) Bonelli, M.; Cestari, C.; Miotello, A. Pulsed Laser Deposition Apparatus for Applied Research. *Meas. Sci. Technol.* **1999**, *10* (3), N27–N30.

(34) Infortuna, A.; Harvey, A. S.; Gauckler, L. J. Microstructures of CGO and YSZ Thin Films by Pulsed Laser Deposition. *Adv. Funct. Mater.* **2008**, *18* (1), 127–135.

(35) Mazzi, A.; Orlandi, M.; Bazzanella, N.; Popat, Y. J.; Minati, L.; Speranza, G.; Miotello, A. Pulsed Laser Deposition of Nickel Oxide Films with Improved Optical Properties to Functionalize Solar Light Absorbing Photoanodes and Very Low Overpotential for Water Oxidation Catalysis. *Mater. Sci. Semicond. Process.* **2019**, *97*, 29–34.

(36) Orlandi, M.; Caramori, S.; Ronconi, F.; Bignozzi, C. A.; Koura, Z. El; Bazzanella, N.; Meda, L.; Miotello, A. Pulsed-Laser Deposition of Nanostructured Iron Oxide Catalysts for Efficient Water Oxidation. *ACS Appl. Mater. Interfaces* **2014**, *6* (9), 6186–6190.

(37) Smith, R. D. L.; Prévot, M. S.; Fagan, R. D.; Trudel, S.; Berlinguette, C. P. Water Oxidation Catalysis: Electrocatalytic Response to Metal Stoichiometry in Amorphous Metal Oxide Films Containing Iron, Cobalt, and Nickel. *J. Am. Chem. Soc.* **2013**, *135* (31), 11580–11586.

(38) Smith, R. D. L.; Prévot, M. S.; Fagan, R. D.; Zhang, Z.; Sedach, P. A.; Siu, M. K. J.; Trudel, S.; Berlinguette, C. P. Photochemical Route for Accessing Amorphous Metal Oxide Materials for Water Oxidation Catalysis. *Science (80-.).* **2013**, *340* (6128), 60–63.

(39) Reece, S. Y.; Hamel, J. A.; Sung, K.; Jarvi, T. D.; Esswein, A. J.; Pijpers, J. J. H.; Nocera, D. G. Wireless Solar Water Splitting Using Silicon-Based Semiconductors and Earth-Abundant Catalysts. *Science (80).* **2011**, *334* (6056), 645–648.

(40) Zou, S.; Burke, M. S.; Kast, M. G.; Fan, J.; Danilovic, N.; Boettcher, S. W. Fe (Oxy)Hydroxide Oxygen Evolution Reaction Electrocatalysis: Intrinsic Activity and the Roles of Electrical Conductivity, Substrate, and Dissolution. *Chem. Mater.* **2015**, *27* (23), 8011–8020.

(41) Du, J.; Chen, Z.; Ye, S.; Wiley, B. J.; Meyer, T. J. Copper as a Robust and Transparent Electrocatalyst for Water Oxidation. *Angew. Chemie*

Int. Ed. **2015**, *54* (7), 2073–2078.

(42) Gorlin, Y.; Chung, C.-J.; Benck, J. D.; Nordlund, D.; Seitz, L.; Weng, T.-C.; Sokaras, D.; Clemens, B. M.; Jaramillo, T. F. Understanding Interactions between Manganese Oxide and Gold That Lead to Enhanced Activity for Electrocatalytic Water Oxidation. *J. Am. Chem. Soc.* **2014**, *136* (13), 4920–4926.

(43) den Daas, H.; Passacantando, M.; Lozzi, L.; Santucci, S.; Picozzi, P. The Interaction of Cu(100)Fe Surfaces with Oxygen Studied by X-Ray Photoelectron Spectroscopy. *Surf. Sci.* **1994**, *317* (3), 295–302. https://doi.org/10.1016/0039-6028(94)90285-2.

(44) Mathieu, H. J.; Landolt, D. An Investigation of Thin Oxide Films Thermally Grown in Situ on Fe24Cr and Fe24Cr11Mo by Auger Electron Spectroscopy and X-Ray Photoelectron Spectroscopy. *Corros. Sci.* **1986**, *26* (7), 547–559. https://doi.org/https://doi.org/10.1016/0010-938X(86)90022-3.

(45) McIntyre, N. S.; Cook, M. G. X-Ray Photoelectron Studies on Some Oxides and Hydroxides of Cobalt, Nickel, and Copper. *Anal. Chem.* **1975**, *47* (13), 2208–2213. https://doi.org/10.1021/ac60363a034.

(46) Li, C. P.; Proctor, A.; Hercules, D. M. Curve Fitting Analysis of ESCA Ni 2p Spectra of Nickel-Oxygen Compounds and Ni/Al2O3 Catalysts. *Appl. Spectrosc.* **1984**, *38* (6), 880–886. https://doi.org/10.1366/0003702844554530.

(47) Bianchi, C. L.; Cattania, M. G.; Villa, P. XPS Characterization of Ni and Mo Oxides before and after “in Situ” Treatments. *Appl. Surf. Sci.* **1993**, *70–71*, 211–216. https://doi.org/https://doi.org/10.1016/0169-4332(93)90429-F.

(48) Mansour, A. N. Characterization of NiO by XPS. *Surf. Sci. Spectra* **1994**, *3* (3), 231–238. https://doi.org/10.1116/1.1247751.

(49) McIntyre, N. S.; Zetaruk, D. G. X-Ray Photoelectron Spectroscopic Studies of Iron Oxides. *Anal. Chem.* **1977**, *49* (11), 1521–1529.

https://doi.org/10.1021/ac50019a016.

(50) Tan, B. J.; Klabunde, K. J.; Sherwood, P. M. A. X-Ray Photoelectron Spectroscopy Studies of Solvated Metal Atom Dispersed Catalysts. Monometallic Iron and Bimetallic Iron-Cobalt Particles on Alumina. *Chem. Mater.* **1990**, *2* (2), 186–191. https://doi.org/10.1021/cm00008a021.

(51) Lian, K. K.; Kirk, D. W.; Thorpe, S. J. Investigation of a “Two-State” Tafel Phenomenon for the Oxygen Evolution Reaction on an Amorphous Ni-Co Alloy. *J. Electrochem. Soc.* **1995**, *142* (11), 3704–3712. https://doi.org/10.1149/1.2048402.

(52) Grosvenor, A. P.; Kobe, B. A.; Biesinger, M. C.; McIntyre, N. S. Investigation of Multiplet Splitting of Fe 2p XPS Spectra and Bonding in Iron Compounds. *Surf. Interface Anal.* **2004**, *36* (12), 1564–1574. https://doi.org/10.1002/sia.1984.

(53) Allen, G. C.; Harris, S. J.; Jutson, J. A.; Dyke, J. M. A Study of a Number of Mixed Transition Metal Oxide Spinels Using X-Ray Photoelectron Spectroscopy. *Appl. Surf. Sci.* **1989**, *37* (1), 111–134. https://doi.org/https://doi.org/10.1016/0169-4332(89)90977-X.

(54) Allen, G. C.; Hallam, K. R. Characterisation of the Spinels MxCo1−xFe2O4 (M = Mn, Fe or Ni) Using X-Ray Photoelectron Spectroscopy. *Appl. Surf. Sci.* **1996**, *93* (1), 25–30. https://doi.org/https://doi.org/10.1016/0169-4332(95)00186-7.

(55) van de Krol, R. Principles of Photoelectrochemical Cells. In *Photoelectrochemical Hydrogen Production*; van de Krol, R.; Grätzel, M. Eds.; Springer US: Boston, MA, 2012; Vol. 102, pp 13–67.

(56) Burke, M. S.; Zou, S.; Enman, L. J.; Kellon, J. E.; Gabor, C. A.; Pledger, E.; Boettcher, S. W. Revised Oxygen Evolution Reaction Activity Trends for First-Row Transition-Metal (Oxy)Hydroxides in Alkaline Media. *J. Phys. Chem. Lett.* **2015**, *6* (18), 3737–3742.

(57) Tilak, B. V; Conway, B. E. Analytical Relations between Reaction Order

and Tafel Slope Derivatives for Electrocatalytic Reactions Involving Chemisorbed Intermediates. *Electrochim. Acta* **1992**, *37* (1), 51–63.

(58) Qiu, J.; Hajibabaei, H.; Nellist, M. R.; Laskowski, F. A. L.; Oener, S. Z.; Hamann, T. W.; Boettcher, S. W. Catalyst Deposition on Photoanodes: The Roles of Intrinsic Catalytic Activity, Catalyst Electrical Conductivity, and Semiconductor Morphology. *ACS Energy Lett.* **2018**, *3* (4), 961–969.

(59) Dalle Carbonare, N.; Cristino, V.; Berardi, S.; Carli, S.; Argazzi, R.; Caramori, S.; Meda, L.; Tacca, A.; Bignozzi, C. A. Hematite Photoanodes Modified with an FeIII Water Oxidation Catalyst. *ChemPhysChem* **2014**, *15* (6), 1164–1174.

(60) Peter, L. M.; Wijayantha, K. G. U.; Tahir, A. A. Kinetics of Light-Driven Oxygen Evolution at α-Fe2O3 Electrodes. *Faraday Discuss.* **2012**, *155* (0), 309–322.

(61) Upul Wijayantha, K. G.; Saremi-Yarahmadi, S.; Peter, L. M. Kinetics of Oxygen Evolution at α-Fe2O3 Photoanodes: A Study by Photoelectrochemical Impedance Spectroscopy. *Phys. Chem. Chem. Phys.* **2011**, *13* (12), 5264–5270.

(62) Dias, P.; Andrade, L.; Mendes, A. Hematite-Based Photoelectrode for Solar Water Splitting with Very High Photovoltage. *Nano Energy* **2017**, *38*, 218–231.

(63) Liardet, L.; Katz, J. E.; Luo, J.; Grätzel, M.; Hu, X. An Ultrathin Cobalt–Iron Oxide Catalyst for Water Oxidation on Nanostructured Hematite Photoanodes. *J. Mater. Chem. A* **2019**, *7* (11), 6012–6020.

(64) Bertoluzzi, L.; Bisquert, J. Equivalent Circuit of Electrons and Holes in Thin Semiconductor Films for Photoelectrochemical Water Splitting Applications. *J. Phys. Chem. Lett.* **2012**, *3* (17), 2517–2522.

(65) Ma, Y.; Le Formal, F.; Kafizas, A.; Pendlebury, S. R.; Durrant, J. R. Efficient Suppression of Back Electron/Hole Recombination in Cobalt Phosphate Surface-Modified Undoped Bismuth Vanadate Photoanodes.

J. Mater. Chem. A **2015**, *3* (41), 20649–20657.

(66) Barroso, M.; Pendlebury, S. R.; Cowan, A. J.; Durrant, J. R. Charge Carrier Trapping, Recombination and Transfer in Hematite (α-Fe2O3) Water Splitting Photoanodes. *Chem. Sci.* **2013**, *4* (7), 2724–2734.

Graphical abstract